

Influence of diffraction on the spectrum and wavefunctions of an open system

J. S. Hersch*, M. R. Haggerty*, and E. J. Heller†

*Department of Physics, Harvard University, Cambridge, Massachusetts 02138

†Departments of Chemistry and Physics, Harvard University, Cambridge, Massachusetts 02138

In this paper, we demonstrate the existence and significance of diffractive orbits in an open microwave billiard, both experimentally and theoretically. Orbits that diffract off of a sharp edge of the system are found to have a strong influence on the transmission spectrum of the system, especially in the regime where there are no stable classical orbits. On resonance, the wavefunctions are influenced by both classical and diffractive orbits. Off resonance, the wavefunctions are determined by the constructive interference of multiple transient, nonperiodic orbits. Experimental, numerical, and semiclassical results are presented.

I. INTRODUCTION

In this work, we discuss the transmission spectrum and wavefunctions of an open resonator coupled to a quantum point contact (QPC). The system exhibits both stable and unstable dynamics, depending on the value of a single parameter. The spectral properties of the resonator are determined by the interference of closed (not necessarily periodic) orbits that begin and end at the QPC. Semiclassically, one computes the transmission of such a system with a sum over the *classical* trajectories. However, it was found experimentally that there were many resonances in the spectrum which did not appear in the theory when classical trajectories involving only specular reflection were considered. We found that the missing resonances were only reproduced when *nonclassical* closed orbits that undergo *diffraction* were included into the semiclassical sum for the transmission.

This issue of including diffraction into the semiclassical propagator has been considered by various authors, for both closed systems [2–4] and open systems [5]. The basis for many of these treatments is the geometric theory of diffraction, originated by Keller [6]. A distinguishing feature of the work presented here is that, in the unstable regime of our resonator, the effect of the diffractive orbits is of the same order as the purely classical orbits. A consequence of this is that there are as many (or more) resonances that are supported by diffractive orbits as are supported by simple classical orbits. This is related to the fact that there is only one classical closed orbit in our system in the unstable regime. This is in stark contrast to the case of a closed, unstable (chaotic) system. Normally, for a closed system, diffraction plays a minor role because of the overwhelming number of nondiffractive periodic orbits present. However, when the system is open, the great majority of long periodic orbits might vanish, if they are allowed to escape the system. In such a case, where only a very small number of classical periodic orbits are present, diffractive orbits may gain in importance and considerably affect the spectrum of the system. This situation is realized by our resonator.

The paper is organized as follows: in Sec. II, we discuss the resonator being studied. In Sec. III, we describe the experimental apparatus. In Sec. IV, we present the experimental results, which are comprised of measured spectra and wavefunctions. In Sec. V we provide a short introduction to the geometric theory of diffraction, which is the theory that describes how diffractive rays contribute to the semiclassical description of a quantum mechanical wavefunction. In Sec. VI we show in detail how the geometric theory of diffraction is incorporated into the semiclassical trace formula. Here theoretical results are seen to be in excellent agreement with measured data. In Sec. VII the physics of the resonator in the time domain is discussed, and again very good agreement between theoretical and experimental observations is found.

In Sec. VIII we discuss the behavior of the system as the transition between stable and unstable dynamics is crossed, as well as analogies of the open resonator with some well-known closed systems, namely the lemon and stadium billiards. Finally, in Sec. IX we discuss the possibility of imaging a pure state quantum mechanical wavefunction in a mesoscopic system with the help of an atomic force microscope, with concluding remarks in Sec. X. A short paper discussing the experimental results presented here has been previously published [7]. See also [8].

II. THE RESONATOR

Recently, Katine studied the transmission behavior of an open quantum billiard in the context of a two dimensional electron gas (2DEG) in a GaAs/AlGaAs heterostructure [9]. Their resonator was formed by a wall with a small aperture (the QPC), and an arc-shaped reflector. A schematic of this resonator is shown in Fig. 1. The voltage on the

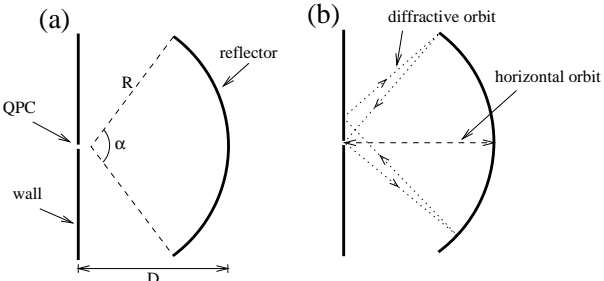


FIG. 1. (a) A schematic of the mesoscopic resonator studied by Katine, with radius of curvature R , opening angle α , and reflector-wall separation D . Electrons impinge on the wall from the left, and the conductance to the region on the right is measured. (b) Two closed orbits of the unstable resonator: diffractive (dotted line), and horizontal (dashed line). These will be discussed later in the paper.

reflector could be varied, effectively moving the reflector towards or away from the wall. Their measurements showed a series of conductance peaks, analogous to those seen in a Fabry-Perot, as the reflector position was varied.

An interesting property of the resonator considered here is that it is geometrically *open*, but in the stable regime it is classically *closed*. In the unstable regime, the resonance properties of the billiard are determined in large part by *diffraction*.

The resonator shown in Fig. 1 has two distinct modes of operation. When the center of curvature of the reflector is to the left of the wall (the regime studied in [9]), then almost all classical paths starting from the QPC that hit the reflector remain forever in the region between wall and the reflector: the dynamics is stable and the periodic orbits can be semiclassically quantized. Each quantized mode of the resonator can be characterized by two quantum numbers (n, m) , which represent the number of radial and angular nodes respectively. As the reflector-wall separation is varied, the conductance exhibits a peak each time one of these quantized modes is allowed. Once an electron is in the resonator, the only way for it to leave is by tunneling back through the QPC or by diffracting around the reflector; since both processes are slow, the resonances have narrow widths. Because the QPC is on the symmetry axis, only modes with even m are excited significantly. The states of the resonator in the stable regime bear a strong resemblance to a certain symmetry class of states in a lemon-shaped billiard [10]. This class has even symmetry about the short axis of the lemon, and odd symmetry about the long axis. This connection will be explored more fully in Section VIII.

When the center of curvature is to the right of the wall, however, the dynamics becomes unstable: all classical trajectories beginning at the QPC rapidly bounce out of the resonator, except for a single unstable periodic orbit along the axis of symmetry, which we will call the “horizontal” orbit [see Fig 1(b)]. The horizontal orbit is a member or a class of orbits that we call “geometric,” because their paths are governed by specular reflection off the wall and reflector, and do not undergo diffraction. Although the horizontal orbit returns to the QPC, the electron has a low probability of escaping the resonator there because the QPC is much smaller than the de Broglie wavelength of the electron. Because the horizontal orbit is the only periodic orbit in the unstable regime, one might expect resonant buildup only along the symmetry axis. Such a spectrum would be quasi-one-dimensional, with only the half-wavelength periodicity of a Fabry-Perot cavity. However, in numerical simulations it was found that there are other transmission resonances in the unstable regime which did not correspond to any classical periodic orbits [11]. It was proposed that these anomalous peaks are supported by diffraction off the tips of the reflector. Unfortunately, in the mesoscopic experiments, decoherence of the electron wave by impurities in the GaAs/AlGaAs heterostructure shortens the lifetime of the resonances, leaving insufficient energy resolution to resolve the diffractive peaks [12].

III. EXPERIMENT

Because of the problems of dissipation and decoherence in the mesoscopic experiments, we decided to investigate a parallel plate microwave resonator with a similar geometry. In microwave experiments, decoherence and dissipation are not a problem, the geometry of the resonator can be specified much more accurately, and the dynamical range of available wavelengths is much larger. The experimental setup is shown in Fig. 2. The equation governing the component of the electric field normal to the plates for the TEM mode is identical to the two-dimensional time-independent Schrödinger equation [13–16]. Therefore, by studying the modes of parallel-plate resonators we can gain insight into the behavior of two-dimensional solutions to the Schrödinger equation.

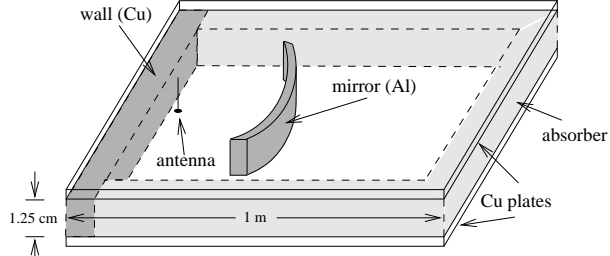


FIG. 2. The microwave analog of the mesoscopic resonator studied by Katine. The antenna simulates the QPC; to reduce its coupling to the resonator, it is placed very close to the wall. The drawing is not to scale.

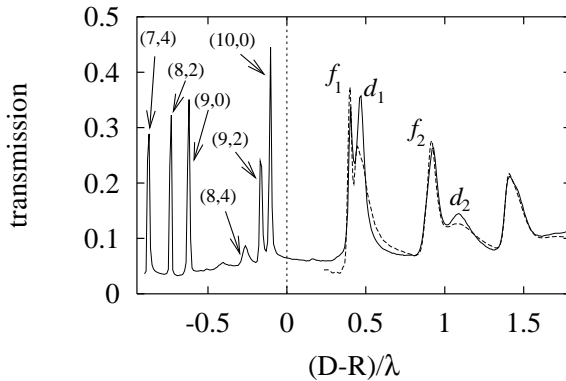


FIG. 3. Experimental transmission versus reflector-wall separation at a fixed frequency of 5.63 GHz; i.e., $R = 5.7\lambda$. The stable/unstable transition point occurs at abscissa zero. In the stable regime, the peaks are labeled by their radial and angular quantum numbers (n, m) . In the unstable regime, the diffractive resonances (labeled d) appear to the right of the Fabry-Perot peaks (labeled f). The dashed curve is the result of a semiclassical calculation which takes diffractive orbits into account (see text). The opening angle for the reflector was $\alpha = 106^\circ$. With the reflector removed from the cavity, the transmission was 0.15 in these units.

The resonator consisted of two parallel copper plates, 1 meter square, separated by a distance of 1.25 cm. One side of the resonator consisted of a copper wall. The other three sides were lined with a 11.5 cm thick layer of microwave absorber (C-RAM LF-79, Cuming Microwave Corp.) designed to provide 20 dB of attenuation in the reflected wave intensity in the range 0.6-40 GHz. The absorber prevented outgoing waves from returning to the resonator, thereby simulating an open system in the directions away from the wall. An antenna was inserted normal to the plates, 2 mm from the wall, to simulate the QPC. The curved reflector was formed from a rectangular aluminum rod bent into an arc with radius of curvature $R = 30.5$ cm. Various opening angles α were used: 115° , 112° , 109° , and 106° .

Instead of measuring the transmission of the resonator, we measured the reflection back from the antenna; for this we used an HP8720D network analyzer in “reflection” mode (the complex S_{11} parameter of the resonator was measured). We inferred the transmission probability $|T|^2$ via $|T|^2 = 1 - |R|^2$, where $R = S_{11}$ is the measured reflection coefficient. Because of the proximity of the antenna to the wall, it was only weakly coupled to the resonator; therefore, in the absence of the reflector, the transmission coefficient was close to zero. However, when the reflector was present, the transmission experienced pronounced maxima at certain frequencies.

IV. RESULTS

In Fig. 3 we show a transmission spectrum at fixed frequency, as the distance between the wall and reflector is varied. In the stable regime, we see that the peaks are narrow and well defined. This is because the dynamics is stable in this regime: nearly all trajectories starting from the QPC that hit the reflector remain forever in the region between the wall and the reflector. In this regime, there exist invariant tori, which may be semiclassically quantized to produce the states of the stable resonator. Such a classical orbit is shown in Fig. 4, along with its quantum mechanical wavefunction counterpart. We see that the trajectory does not approach the region where the resonator is open. Thus, it behaves as if the cavity were *closed*—hence the narrow widths of the peaks in the stable regime.

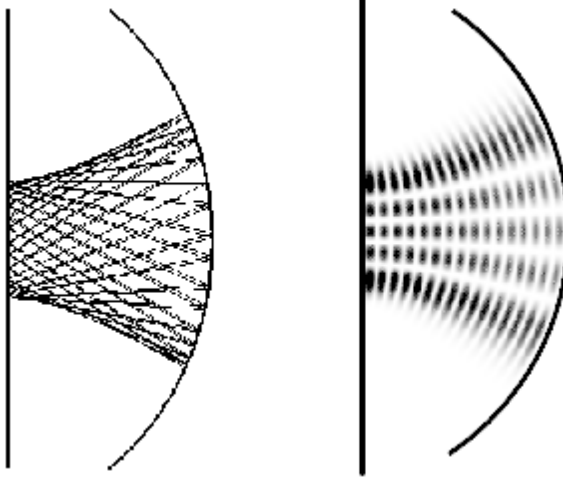


FIG. 4. On the left is a classical trajectory starting at the QPC. On the right is the corresponding computed wavefunction.

In the unstable regime, the transmission curve is quite different. Here, there are two types of resonances. The first type, labeled f in Fig. 3, is related to the horizontal orbit along the axis of symmetry, and bears some resemblance to a Fabry-Perot type resonance between two half-silvered mirrors. The second type, labeled d , is supported by diffraction off the tips of the reflector.

We verified experimentally that the d -peaks were indeed supported by diffraction by surrounding the tips of the reflector with microwave absorber and repeating the experiment, as indicated in Fig. 5. When this was done, the Fabry-Perot resonances were unaffected, but the diffractive peaks were entirely eliminated from the spectrum. This makes sense because the gradually thickening absorber smoothly attenuated reflections from rays coming near the tip, leaving no sharp discontinuity from which rays could diffract.

The wavefunctions corresponding to peaks f_1 and d_1 were measured using the technique of Maier and Slater [17]. They showed that the frequency shift of a given resonance due to a small sphere of radius r_0 at a position (x, y) is given by

$$\frac{\omega^2 - \omega_0^2}{\omega_0^2} = 4\pi r_0^3 \left(\frac{1}{2} H_0^2(x, y) - E_0^2(x, y) \right), \quad (1)$$

where E_0 and H_0 are the unperturbed electric and magnetic fields. Thus, the frequency shift is proportional to the local intensity of the microwave field, and by measuring the shift as a function of the position of the sphere, the field intensity of a particular mode can be mapped out. Note that the frequency shift is positive in regions where the magnetic field is large, and negative where the electric field is large. Also, the factor of 1/2 multiplying the magnetic field in Eq. (1) indicates that the sphere is a stronger perturbation to the electric field than the magnetic field. In our measurements, we found this to be the case: the shifts were predominantly negative. Appreciable positive shifts were found only at the nodes of the electric field, corresponding to maxima of the magnetic field.

Figure 6 shows theoretical quantum wavefunctions compared with experimentally measured frequency shifts for the resonances labeled by f_1 and d_1 in Fig. 3. The theoretical wavefunctions were generated using Edwards' wavelet method presented in [11]. The measured frequency shift is plotted as a function of sphere position. For these measurements, we used a steel bead of diameter 4.0 mm for the perturbation. The bead was rastered over the inside of the cavity by means of an external magnet. That way, the bead could be moved around inside the cavity without taking the cavity apart. It is important to note that the frequency shift is not proportional to E^2 , but rather to $H^2/2 - E^2$. Therefore we show only negative contour lines below 20% of the maximum negative shift, and thereby emphasize regions of strong electric field. The similarity between theory and experiment is striking.

The wavefunction labeled f_1 in Fig. 6 is clearly associated with the horizontal orbit along the axis of symmetry. Rays emanating from a point source located on the axis of symmetry next to the wall bounce off the reflector and come to an approximate focus about 10 cm from the source. The focus is approximate because of spherical (or in this case cylindrical) aberration.

Now we turn our attention to the state labeled d_1 in Fig. 6. As noted above, the only periodic orbit in the unstable regime is the horizontal orbit, along the axis of symmetry. The pictured wavefunction, however, clearly has very

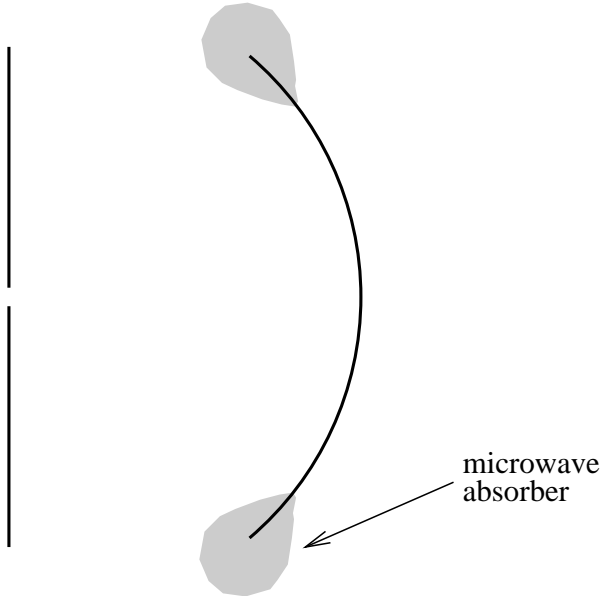


FIG. 5. Diffractive peaks could be removed from the spectrum by placing microwave absorber near the tips of the reflector, as indicated.

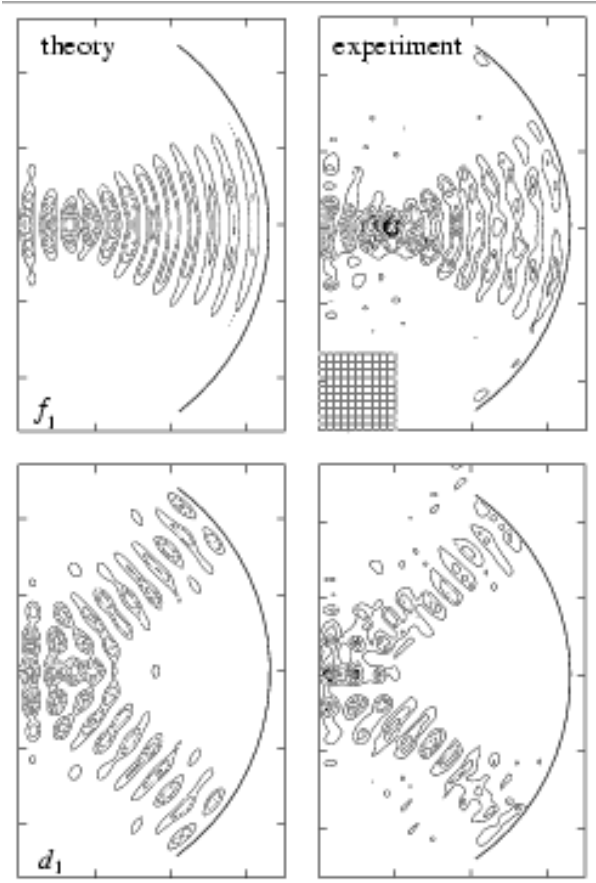


FIG. 6. Comparison between theoretical quantum wavefunctions (left) and experimentally measured microwave frequency shifts (right). The two modes correspond to peaks f_1 and d_1 , respectively, in Fig. 3. The wall is located on the left vertical axis in each plot, and the reflector position is indicated by the arc. The graph ticks are 10 cm apart. The fine grid indicates the spacing of the experimentally sampled points (grid spacing 1 cm).

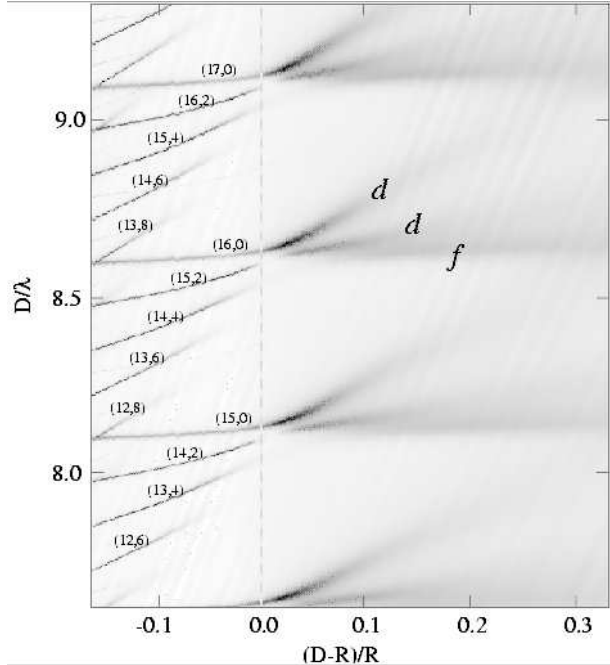


FIG. 7. Experimental transmission versus reflector-wall separation and wavelength. High transmission regions are dark. On the left of the vertical dotted line is the stable regime, where the transmission peaks are sharp. The quantum numbers (n, m) are indicated for many of the peaks. On the right is the unstable regime, where the resonances become wider and diffractive orbits become important. Transmission peaks supported by diffractive orbits are marked by d .

little amplitude along this periodic orbit. Instead the wavefunction has a band of higher amplitude running from the region of the tip of the mirror to the QPC, but in the unstable regime there is no *classical* periodic orbit that does this. Later in the paper, it will be shown that states such as d_1 are supported by orbits that undergo *diffraction* off the tips of the reflector. One such orbit is shown in Fig. 1(b). Rays that hit the smooth surfaces of the reflector or wall undergo specular reflection, whereas the rays that hit near the reflector tips can be diffracted. A fraction of the wave amplitude can then return to the QPC from this region, thus setting up a *non-classical* closed orbit. All peaks labeled with a d in Fig. 3 are supported by such diffractive orbits.

Numerical calculations have shown that for energies off resonance, the quantum wavefunction is often intermediate between those shown for f_1 and d_1 , in the sense that amplitude seems to be running from the QPC to some point between the center and the tip of the reflector [11].

This can be understood in terms of the interference of paths with each other as they “walk off” the horizontal orbit and escape the resonator. Thus diffraction does not necessarily play a major role in determining the off-resonance wavefunctions. However, diffraction *is* instrumental in determining the on-resonance wavefunctions underlying the conductance peaks d_1 and d_2 in Fig. 3. Figure 7 shows a more global picture of the transmission properties of the resonator. Here we plot the transmission of the resonator as both the wavelength and the reflector-wall separation are varied. Each vertical slice through this figure is a frequency spectrum with fixed reflector position; the dotted line marks the classical transition from stable to unstable motion that occurs when the reflector’s center of curvature moves to the right of the QPC. The vertical axis indicates how many wavelengths fit along the horizontal orbit between the QPC and the reflector. The repetition of the resonance pattern every half-wavelength in the vertical direction is analogous to the half-wavelength periodicity of a Fabry-Perot cavity.

In the stable regime the peaks have been labeled with their quantum numbers, (n, m) . Because of the choice of vertical axis, the $m = 0$ resonance peaks are approximately horizontal in this figure. As the stable/unstable transition is approached, the peaks with high m disappear one by one because their large angular sizes allow them to escape around the reflector.

At the stable/unstable transition, all of the resonances in a family would be approximately degenerate, but instead there is an avoided crossing. The level repulsion is caused by a coupling that is partly mediated by diffraction; this subject will be explored more thoroughly in Section VIII.

In Fig. 8 the angular dependence of a diffractive state is shown as the reflector is passed adiabatically through the stable/unstable transition point. In the stable region, most of the amplitude is along the symmetry axis. As the reflector moves further from the wall, the amplitude slowly separates into two lobes, with very little in the center.

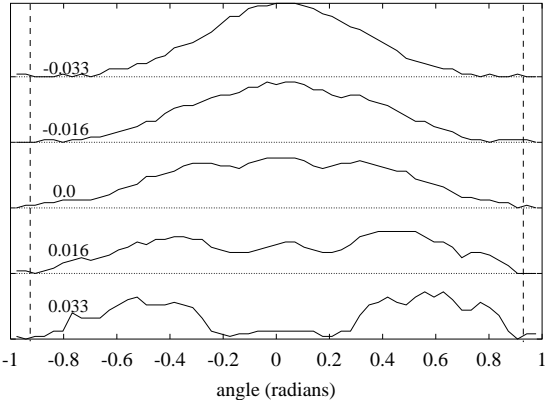


FIG. 8. In this figure, we show the angular dependence of a diffractive state as the reflector is moved through the stable/unstable transition. Plotted is the amplitude of the frequency shifts measured 1 cm away from the reflector. The value of $(D - R)/R$ is indicated for each curve. The tips of the reflector are indicated on the plot by vertical dashed lines.

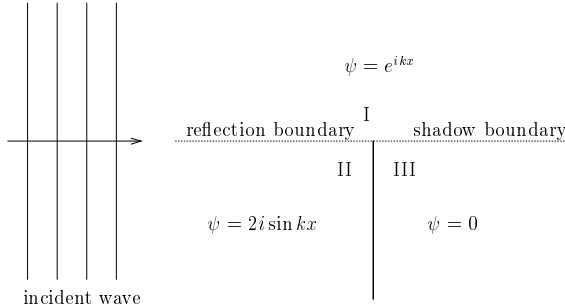


FIG. 9. Diffraction from an infinite half-line in 2D.

When the reflector is only slightly in the unstable region, there are bands of amplitude running to a point on the reflector intermediate between the center and the tips, as in the curve for $(D - R)/R = 0.016$ in Fig. 8.

In the unstable regime, the only remaining classical periodic orbit is the horizontal orbit, which itself becomes unstable. The Fabry-Perot peak (labeled f) is essentially quantized along the horizontal orbit, so its position shows a simple dependence on reflector position. It becomes broad in the unstable regime, with a lifetime given by the classical Lyapunov stability exponent of the horizontal orbit. Two diffractive resonances (labeled by d), are also visible in each family; they separate from the Fabry-Perot type peak as the reflector is moved away from the wall.

The diffractive peaks labeled by d in Fig. 7 cannot be explained by semiclassical theory unless diffraction off the tips of the reflector is included, as will be shown in the following sections.

V. GEOMETRIC THEORY OF DIFFRACTION

Before we consider the problem of computing semiclassically the transmission properties of our resonator, let us study the simpler problem of diffraction of a plane wave off an infinite half-line in 2D. This problem will serve as a good introduction into the geometrical theory of diffraction, which will be used to include diffraction into the semiclassical propagator.

The problem is illustrated in Fig. 9. A plane wave e^{ikx} is normally incident on the half-line from the left. The half-line extends up from the middle of the figure, indicated by the dark line. We take the tip of the line to be our coordinate origin. Within the geometrical optics approximation, the problem is divided into three separate regions: that of transmission, reflection, and shadow, labelled I, II, and III, respectively. The values of the wavefunction in each region are indicated in the figure as well. In region I, the wave does not hit the wall and thus is unchanged

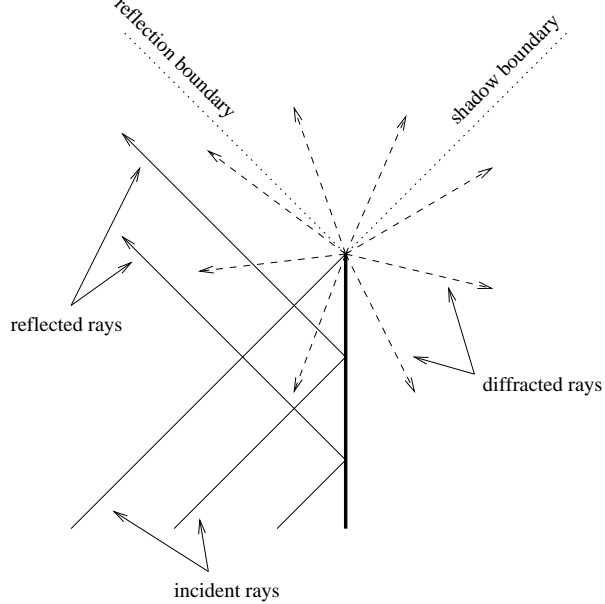


FIG. 10. Reflected and diffracted rays from an infinite half-line. Diffracted rays are shown in dashed lines. The reflection and shadow boundaries are indicated. The wave is incident from the lower left corner of the figure, as indicated by the incident rays.

within the geometric optics approximation. In region II, the wave is perfectly reflected and thus a standing sine wave is set up there. In region III, we have a perfect shadow region, which is completely dark. Along the reflection and shadow boundaries indicated, the solution is discontinuous. Of course, these discontinuities are not present in the exact solution; they are an artifact of the geometric approximation. As we shall see, it is the diffraction off the tip of the wall that corrects these discontinuities.

In 1953, Keller showed that one can think of diffraction as originating from a group of “diffracted rays” originating from the edge of the wall [6]. The idea is illustrated in Fig. 10. Away from the shadow and reflection boundaries, these diffracted rays have the form of an outgoing cylinder wave, multiplied by an angle dependent “diffraction coefficient.” However, Keller’s original theory was shown to be invalid on the reflection and shadow boundaries. A properly uniformized geometric theory of diffraction was developed by Kouyoumjian and Pathak [20]. The diffracted rays are multiplied by a suitable complex number which depends both on the angles of the incident and diffracted rays relative to the wall, as well as the distance from the edge. In this uniformized theory, the solution to the half-line is given by

$$\psi(\mathbf{r}) = \psi_g(\mathbf{r}) + D(\theta, \theta', r, k) e^{ikr}, \quad (2)$$

where $\psi_g(\mathbf{r})$ is the solution given by geometrical optics, shown in Fig. 9. The diffraction coefficient $D(\theta, \theta', r, k)$ is given by [18,19],

$$D(\theta, \theta', r, k) = -\text{sgn}(a_i) K(|a_i| \sqrt{kr}) + \text{sgn}(a_r) K(|a_r| \sqrt{kr}), \quad (3)$$

$$a_{i,r} = \sqrt{2} \cos\left(\frac{\theta \mp \theta'}{2}\right), \quad (4)$$

and $K(x)$ is a modified Fresnel integral:

$$K(x) = \frac{1}{\sqrt{\pi}} e^{-ix^2 - i\pi/4} \int_x^\infty e^{it^2} dt. \quad (5)$$

The angles θ, θ' are shown in Fig. 11. In the half-line problem, $\theta = \pi/2$, because the incident wave is normal to the wall. In addition, in Eq. (2) we understand that the origin of the coordinate system is at the tip of the half-line.

In Fig. 12 we compare the result of Eq. (2) to the exact solution for the half-line. The prediction of geometric optics is also shown. There is very good agreement between the exact solution and the uniform geometric theory. Note

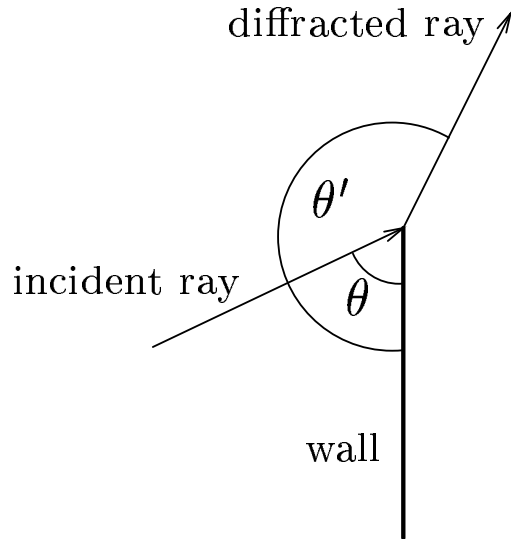


FIG. 11. Angles of the incident and diffracted ray for use in Eq. (3).

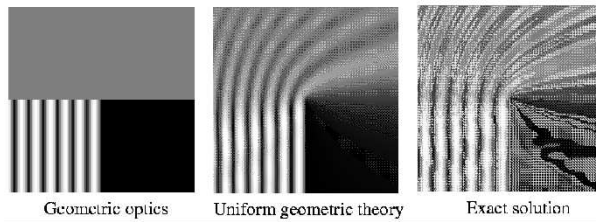


FIG. 12. Comparison of the geometric optics approximation, the uniform geometrical theory, and the exact solution for the diffraction of quantum particle off an infinite half-line screen. The screen extends from the lower center to the center of the picture. Plotted is the norm of the wavefunction, $|\psi|$. Note the stark discontinuities on the shadow and reflection boundaries in the geometric optics approximation. Regions of high probability amplitude are light.

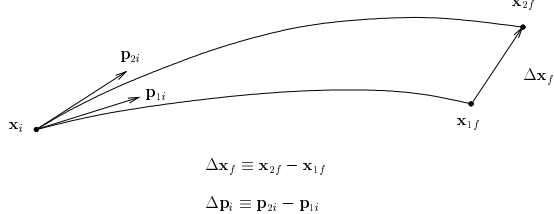


FIG. 13. Two trajectories launched from the same point with slightly different momenta \mathbf{p}_{1i} and \mathbf{p}_{2i} . Each momentum has the same magnitude; only the directions are different. The labels i, f stand for initial and final.

especially that the discontinuities on the shadow and reflection boundaries are completely removed by the uniform theory.

VI. SEMICLASSICS IN THE ENERGY DOMAIN

Now we turn back to the problem of calculating the transmission properties of our resonator. We need to find an expression for the Green function for the resonator, because the transmission can be easily written in terms of the diagonal part of the energy Green function [22]:

$$T(E) \propto \text{Re} [iG(\mathbf{r}_{\text{QPC}}, \mathbf{r}_{\text{QPC}}, E)], \quad (6)$$

where \mathbf{r}_{QPC} is the center of the QPC. The physical reason that $G(\mathbf{r}_{\text{QPC}}, \mathbf{r}_{\text{QPC}}, E)$ appears in Eq. (6) is because all waves enter our resonator within a fraction of a wavelength of that point. If a point source of waves is launched at \mathbf{r}_{QPC} with energy E , the complex number $G(\mathbf{r}_{\text{QPC}}, \mathbf{r}_{\text{QPC}}, E)$ is just the amplitude for returning to \mathbf{r}_{QPC} . If a significant fraction of the rays emanating from the point source return to \mathbf{r}_{QPC} in phase, then $G(\mathbf{r}_{\text{QPC}}, \mathbf{r}_{\text{QPC}}, E)$ will be appreciable, and the returning waves will beat against the original wave and have a large effect on the transmission.

1

A. Geometric orbits in the semiclassical propagator

The 2D semiclassical energy Green function $G_{\text{sc}}(\mathbf{r}, \mathbf{r}', E)$ can be written as a sum over paths from \mathbf{r} to \mathbf{r}' thus [1]:

$$G_{\text{sc}}(\mathbf{r}, \mathbf{r}', E) = \frac{2\pi}{(2\pi i)^{3/2}} \sum_{\text{paths}} \frac{1}{\sqrt{A}} \exp [iS(\mathbf{r}, \mathbf{r}') - i\pi\mu/2], \quad (7)$$

where $S(\mathbf{r}, \mathbf{r}')$ is the action and μ is the Maslov index for the path. The stability coefficient A is given by

$$A = \frac{\partial \mathbf{x}_{\perp f}}{\partial \mathbf{p}_i} = \lim_{\Delta \mathbf{p}_i \rightarrow 0} \frac{\Delta \mathbf{x}_{\perp f}}{\Delta \mathbf{p}_i}, \quad (8)$$

using the definitions from Fig. 13, and where $\Delta \mathbf{x}_{\perp f}$ is the component of $\Delta \mathbf{x}_f$ that is perpendicular to \mathbf{p}_{1f} . The coefficient A describes the stability of trajectories beginning from a particular point in phase space. If A is large, then small changes in the initial direction of the trajectory lead to large displacements in the final positions. More precisely, if the distance $\Delta \mathbf{x}_{\perp f}$ grows exponentially with the length of the trajectories, we say that the trajectories are chaotic. If $\Delta \mathbf{x}_{\perp f}$ grows only linearly, then they are stable.

For the case of our resonator in the unstable regime, only one type of orbit enters into the sum in Eq. (7): the horizontal orbit. Therefore, in order to find the contributions of the geometric orbits to the transmission spectrum, we need only the actions ($S = kl$, where l is the length of the orbit) and stability coefficients A for the primary horizontal orbit and its repetitions. In addition, we need to keep track of the Maslov index for each orbit. A series of such orbits, together with the associated Maslov indices, is shown schematically in Fig. 14(a). In this figure, the QPC/wall is located at the lower part of each diagram, while the reflector is located at the upper part. Each upward (downward) sloping line segment represents part of a trajectory from the QPC (reflector) to the reflector (QPC).

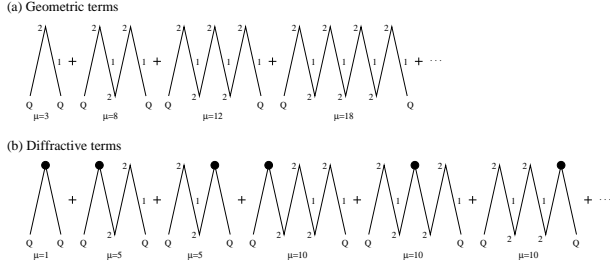


FIG. 14. Diagrams of orbits included into the semiclassical Green function in Eq. (7). In (a), the horizontal orbits are shown. The upper vertices represent bounces off the reflector, while the lower vertices signify reflections off the QPC. The Maslov indices are shown for each part of each orbit, and the total index is given below each diagram. In (b), the diffractive orbits are shown. The filled circle represents a diffraction event, where the term is multiplied by the diffraction coefficient, D . After a diffractive event, the return path does not acquire a Maslov index of 1, because it is a diffracted ray; only the specularly reflected rays participate in the caustic.

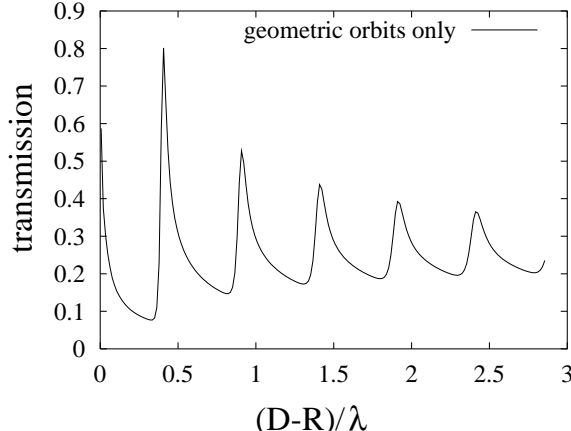


FIG. 15. Semiclassical transmission including only the geometric orbits. The data is for fixed energy, corresponding to $kR = 40$, with the distance between the wall and reflector varied along the x -axis.

Maslov indices of $\mu = 2$ are indicated for points where the wave is reflected at the wall or arc-reflector, and an index of $\mu = 1$ is acquired each time the ray passes through the focus on its return from the reflector toward the wall.

Figure 15 shows a transmission spectrum for the resonator in the unstable regime, computed using only the horizontal orbit. For this calculation, the sum in Eq. (7) was cut off after the 20th term, that is, orbits of up to 20 round trips were included in the sum. The half-wavelength periodicity of the spectrum is clearly seen in the figure. Upon comparison with Fig. 3, we see that the peak positions match very well with the experimentally measured spectrum. Note, however, the absence of the peaks corresponding to diffractive orbits which are present in Fig. 3. It is to the calculation of these diffractive resonances that we now turn.

B. Diffractive orbits in the semiclassical propagator

So far, the Green function in Eq. (7) includes paths that undergo evolution under the free-particle Hamiltonian, including bounces off the wall and mirror. In order to calculate the spectral properties of the resonator semiclassically, diffractive orbits must be included into the sum over paths that forms the semiclassical propagator. This problem has been studied by a number of authors [2–4]. In the literature, much attention has been focused on finding the effects of diffraction on the spectra of closed systems. However, in closed systems, diffractive orbits generally play a minor role because they are overwhelmed by the huge number of unstable periodic orbits that do not involve diffraction. In this section, these methods will be extended to include open systems.

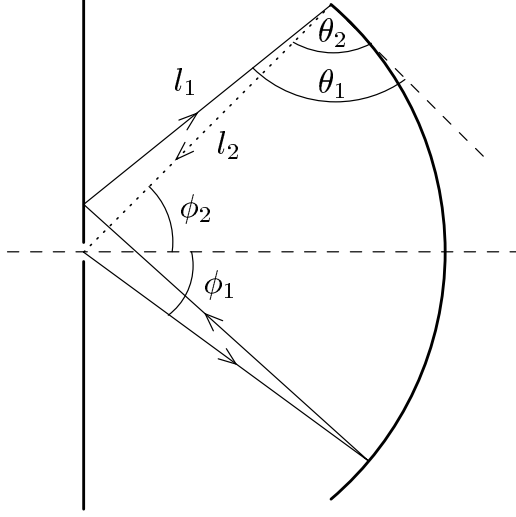


FIG. 16. Here is shown the various angles relevant to a particular diffractive orbit entering into the semiclassical Green function in Eq. (9). The first leg of the orbit, l_1 , is drawn with a solid line, and the second leg, l_2 , is drawn with a dotted line. This orbit corresponds to the third term in the sum shown in Fig. 14(b).

For our purposes, it is sufficient to include diffraction at the level of a single diffraction event per orbit. Although multiply diffracted orbits strictly belong in the semiclassical sum, in practice they can be safely neglected. This is because of the amplitude of an incident ray on the reflector tip is subsequently sprayed in all directions, so that only a small part returns in a direction that eventually leads it back to the QPC. Therefore, we will consider only singly diffracted orbits. The Green function is the product of three amplitudes: the first for going from the starting point to the point of diffraction, the second for the diffraction event itself, and the third for going from the diffraction point to the final point, as follows:

$$\begin{aligned} G_{\text{diff}}(\mathbf{r}, \mathbf{r}', E) &= G_{\text{sc}}(\mathbf{r}, \mathbf{r}_d, E) D(l_1, l_2, \theta_1, \theta_2, E) G_{\text{sc}}(\mathbf{r}_d, \mathbf{r}', E) \\ &= -\frac{1}{2\pi i} \sum_{\text{paths}} \frac{D(l_1, l_2, \theta_1, \theta_2, E)}{\sqrt{A_1 A_2}} \cos \phi_1 \cos \phi_2 \exp [i(S_1 + S_1) - i\pi(\mu_1 + \mu_2)/2], \end{aligned} \quad (9)$$

where the diffraction event occurs at position \mathbf{r}_d , and the total path from \mathbf{r} to \mathbf{r}' is made up of two legs, one of length l_1 , with stability coefficient A_1 , and the other of length l_2 , with stability coefficient A_2 . Each of these legs has an action $S_1 = kl_1$, $S_2 = kl_2$ and Maslov index μ_1, μ_2 associated with it. The factors $\cos \phi_1, \cos \phi_2$ represent the coupling of each leg to the QPC, and will be discussed in the next section. The various parameters are illustrated in Fig. 16 for one of the shorter orbits, corresponding to the third term in Fig. 14(b). In that figure, the first few terms entering into Eq. (9) are shown, where diffraction events are represented by filled circles.

The diffraction coefficient $D(l_1, l_2, \theta_1, \theta_2, E)$ depends on the lengths of each leg as well as the angles that the incident and diffracted ray make with the surface at the tip of the obstacle. These various lengths and angles are shown in Fig. 16. The diffraction coefficient in the sum above is similar to that appearing in our study of the half-line, differing only in the argument of the Fresnel integral. It is given by,

$$\begin{aligned} D(\theta_1, \theta_2, l_1, l_2, k) &= -\text{sgn}(a_i) K \left(|a_i| \sqrt{\frac{kl_1 l_2}{l_1 + l_2}} \right) + \text{sgn}(a_r) K \left(|a_r| \sqrt{\frac{kl_1 l_2}{l_1 + l_2}} \right), \\ a_{i,r} &= \sqrt{2} \cos \left(\frac{\theta_1 \mp \theta_2}{2} \right), \end{aligned} \quad (10)$$

and $K(x)$ is the modified Fresnel integral defined in Eq. (5).

The effect of the diffractive terms in the sum is shown in Fig. 17. For this calculation, all orbits with up to 20 round trips between the wall and mirror and zero or one diffractive events were included in the sum. We see that the effect

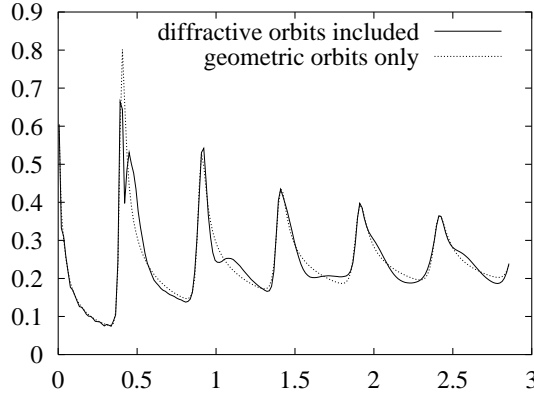


FIG. 17. Semiclassical transmission including both the geometric and diffractive orbits. The data is for fixed energy, corresponding to $kR = 40$, with the distance between the wall and reflector varied along the x -axis. The result without diffraction is shown with a dashed line for comparison.

of the diffractive terms is to modulate the geometric result, with new peaks appearing to the right of the geometric peaks. The theoretical curve appearing in Fig. 17 is overlaid with the experimental data in Fig. 3; the agreement between theory and experiment is quite good, both in the peak positions and widths of the geometric and diffractive peaks. We emphasize here that the semiclassical prediction breaks down for reflector/wall separations near $D = R$, because there the focus approaches the point where the Green function is evaluated, and the semiclassical prediction diverges. This is the reason for the incorrect, large transmission calculated at $D = R$.

In Fig. 18, we plot the semiclassically calculated transmission of the resonator in the unstable regime versus both reflector/wall separation and wavelength. The parameters are identical to those of the experimental data shown in Fig. 7. The separation of the diffractive peaks from the Fabry-Perot peaks with increasing reflector/wall separation is quite clear. Two diffractive peaks per geometric peak are visible. The half-wavelength periodicity is also apparent. The similarity between theory and experiment in these two figures is striking.

C. Semiclassical wavefunctions

In this section, we describe the procedure for including diffraction into a semiclassical calculation of the resonator wavefunctions. As in the previous sections, we can split up the sum over paths into a geometric part and a diffractive part. The contribution to ψ from the geometric orbits is proportional to the semiclassical amplitude for getting from the QPC to the point of interest:

$$\psi_{\text{geo}}(\mathbf{r}) \propto G_{\text{sc}}(\mathbf{r}_{\text{QPC}}, \mathbf{r}, E), \quad (11)$$

where \mathbf{r}_{QPC} is the location of the QPC, and \mathbf{r} is the location of interest. This Green function is the same as we have already encountered in the semiclassical expression for the transmission neglecting diffraction, appearing in Eqs. 6 and 7. The only difference is that now we are looking at an off-diagonal element of the Green function, rather than a diagonal element. Some of the shorter trajectories that are included in the sum are shown in Fig. 19(a). All such trajectories begin at the QPC and end at the point \mathbf{r} , undergoing specular reflection at the wall and reflector.

To include diffraction, we simply add diffractive terms to the sum, much as we did to incorporate the effects of diffraction in the formula for the Green function in Eq. 9. We have

$$\psi(\mathbf{r}) \propto G_{\text{sc}}(\mathbf{r}_{\text{QPC}}, \mathbf{r}, E) + G_{\text{sc}}(\mathbf{r}_{\text{QPC}}, \mathbf{r}_{\text{tip}}, E)D(l_1, l_2, \theta_1, \theta_2, E)G_{\text{sc}}(\mathbf{r}_{\text{tip}}, \mathbf{r}, E), \quad (12)$$

where the diffraction coefficient $D(l_1, l_2, \theta_1, \theta_2, E)$ is identical to that appearing in Eq. 10. The lengths l_1, l_2 and angles θ_1, θ_2 are defined the same way as in Fig. 16, with the obvious difference that the final point of the trajectory is no longer the location of the QPC, but the location of interest, \mathbf{r} . In Fig. 20 we show the result of a semiclassical calculation for the wavefunctions pictured in Fig. 6. For comparison, we also show the result when diffractive paths are left out of the sum. In the calculation, all singly diffracted paths involving up to 20 bounces were included.

We saw earlier that diffraction has a large effect on the transmission spectrum, which in turn could be derived from the value of the wavefunction near the QPC. By contrast, we see now that the inclusion of diffraction has a relatively

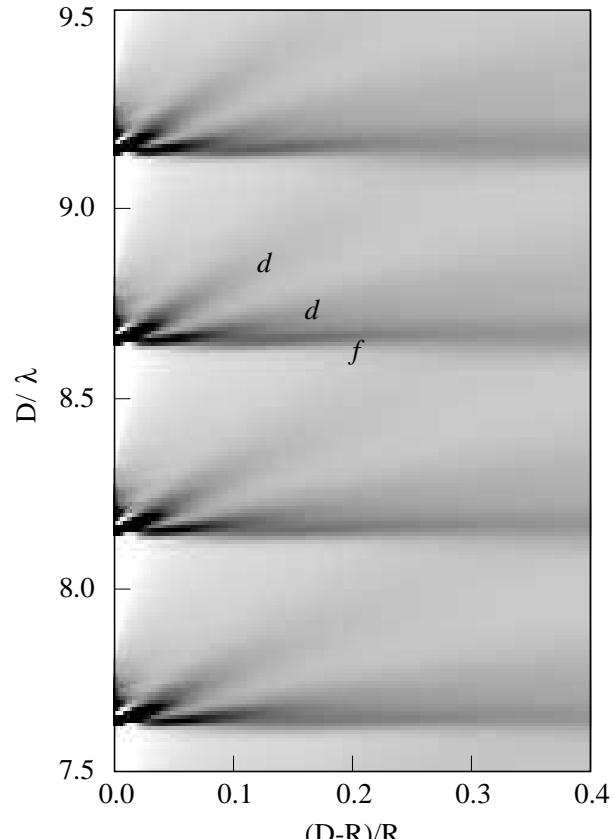


FIG. 18. Semiclassical conductance of the resonator versus wavelength and reflector position in the unstable regime. The plot is exactly analogous to the experimental data shown on the right side of Fig. 7. Note that the semiclassical prediction breaks down near $D = R$ (see text).

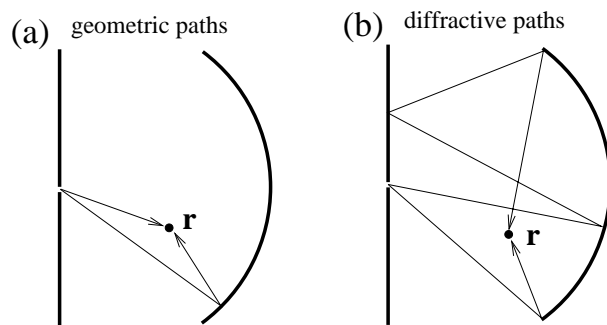


FIG. 19. In (a), the two shortest geometric trajectories from the QPC to the point \mathbf{r} are shown. Such orbit are specularly reflected off the wall and mirror. In (b), the two shortest diffractive trajectories from the QPC to the point \mathbf{r} are drawn.

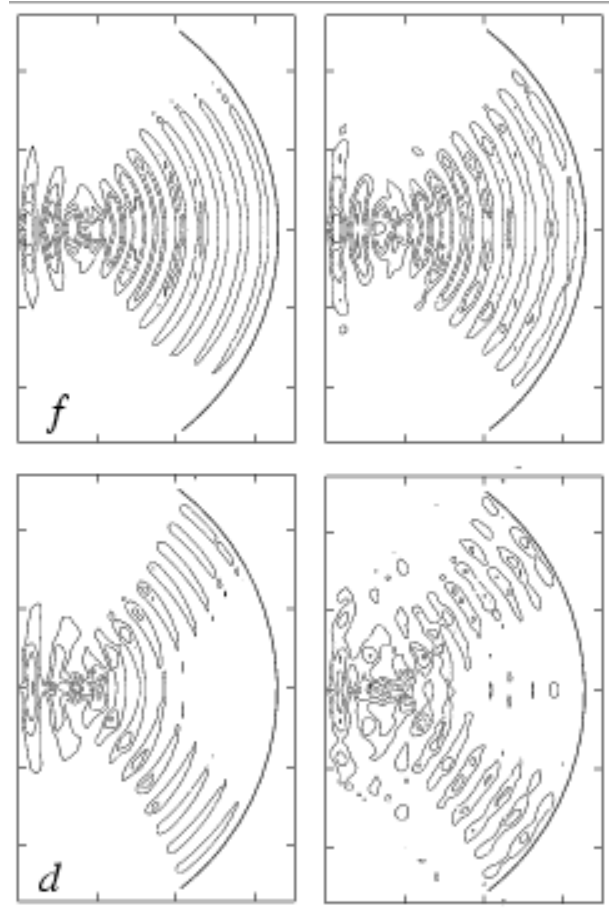


FIG. 20. Two wavefunctions calculated semiclassically. On the left, only the geometric paths were included in the sum; on the right trajectories that diffract off the edges of the reflector were taken into account. These plots are for identical parameter sets as those shown in Fig. 6.

minor effect on the overall appearance of the wavefunctions. The explanation for this apparent paradox is that the QPC is near many reflection boundaries, where the diffractive corrections are especially large.

The transmission through a small aperture (here the QPC) is extremely sensitive to small returning bits of amplitude, which interfere coherently with the wave entering through the aperture to modulate the transmission. In our case, a major source of returning amplitude is provided by the diffractive orbits. This is analogous to scanning tunneling microscope “quantum corral” imaging [23], where the tunneling from the tip plays the role of the quantum point contact, and reflections from atoms and impurities represent the diffraction and geometric scattering off the ends of the reflector. The modulation of the transmission through the QPC by the presence of the reflector can be understood in terms of a small returning wave amplitude beating against a much stronger “nascent” amplitude coming out of the QPC: if the amplitude from the QPC in absence of the reflector is A , and the returning amplitude with the reflector present is a , then the total amplitude at the QPC is simply $A + a$. The transmission will be proportional to the square of this amplitude,

$$T \propto |A + a|^2 = |A|^2 + aA^* + a^*A + |a|^2. \quad (13)$$

The two interference terms above, linear in a , are responsible for all the structure in the transmission when the reflector is present in the cavity.

VII. SEMICLASSICS IN THE TIME DOMAIN

Further evidence of diffractive orbits in the transmission spectrum can be obtained by analyzing the spectrum in the time domain. The two representations are related by the Fourier transform:

$$g(t) = \int_{-\infty}^{\infty} S_{11}(\omega) e^{i\omega t} dt. \quad (14)$$

Here $g(t)$ represents the amplitude for a pulse launched from the QPC at time $t = 0$ to return at time t . That is, if a short pulse were emitted from the antenna at time $t = 0$, echos would return to the antenna at certain later times. These echos are indicated by peaks in the return spectrum. In Fig. 21, we plot the amplitude $|g(t)|$ as a function of time for the resonator in the stable and unstable regimes. In these plots, time has been normalized so that one unit is the time it takes for light to travel a distance equal to the radius of curvature of the reflector. In the stable regime, the echos persist for hundreds of bounces, indicating that indeed the dynamics is stable in this regime. In this regime, the lifetime of the states is limited by resistive losses in the copper plates of the resonator, which was quite small: typical quality factors of the resonances in this regime were $Q \sim 3000$. However, in the unstable regime, the echos are significantly reduced in amplitude after only a few returns. For the first few return peaks, $|g(t)|^2$ decays exponentially with a decay constant given approximately by the Lyapunov exponent for the horizontal orbit. Later peaks, where diffractive orbits are more important, also decay exponentially but with a different decay constant.

In Fig. 22, we show an expanded view of some of the return peaks shown in Fig. 21(b). Of importance here is the splitting of the return peaks which is visible on echos 5-9. This splitting is due to the coexistence of orbits with slightly different periods. The longer of these orbits is just the horizontal orbit, which appears on the right of each group. The left peak of each group is made up of a family of diffractive orbits of nearly the same length. We have done a quantitative study of the lengths of the closed orbits and find excellent agreement with the observed splitting. The calculated lengths of the orbits appear in the plot as vertical bars above the peaks. The horizontal orbit length is marked with a longer bar. The lengths of all the orbits in units of the radius of curvature appear in Table. I. The presence of this splitting in the return spectrum is strong evidence in support of the claim that diffraction off the edges of the reflector supports other closed orbits, which lead to resonances in the transmission spectra. Note that for the long orbits, the diffractive peaks are even stronger than the peaks from the geometric orbit. This is because the number of diffractive orbits increases linearly with the length of the orbit, whereas there is always only one geometric orbit, regardless of length.

VIII. THE AVOIDED CROSSING

We now turn our attention to the avoided crossing that appears in Fig. 7 near $(D - R)/R = 0$. We mentioned earlier that the level repulsion at this point is in part mediated by diffraction. To show this, we compare our open resonator with three closely-related closed systems.

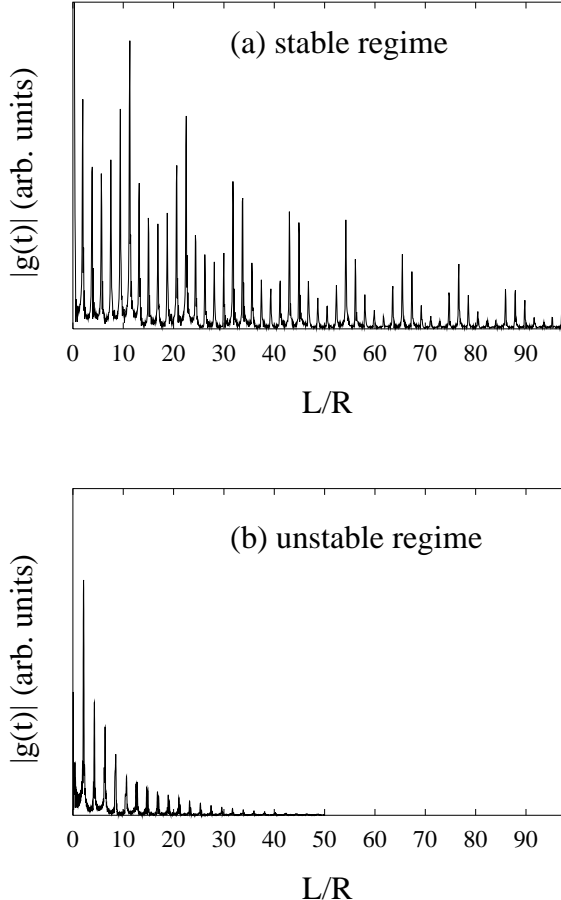


FIG. 21. Experimental return spectra in the (a) stable and (b) unstable regime. Time has been converted to the ratio L/R , where L is the length of the orbit. For these plots the opening angle was 115° , and the reflector-wall separation was 28.5 cm and 32.5 cm, respectively. For the unstable case, the theoretically predicted envelope of the decay given by the Lyapunov exponent is shown as well.

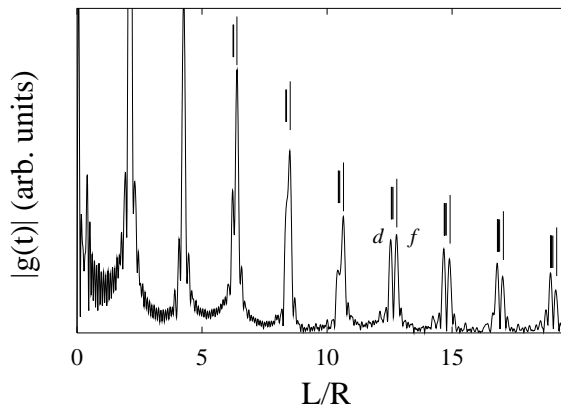


FIG. 22. Experimental return spectra for the unstable regime. Time has been converted to the ratio L/R , where L is the length of the orbit. The splitting of the peaks clearly demonstrates the influence of both Fabry-Perot type orbits (marked f) and diffractive orbits (marked d), which are slightly shorter. The calculated lengths of the orbits are shown by vertical bars; short bars for the diffractive orbits, and longer bars for the horizontal orbit. For these plots the opening angle was 115° , and the reflector/wall separation was 32.5 cm.

Lengths of diffractive orbits							
N	N_1	N_2	L_1	L_2	L_{tot}	L_{hor}	Δ
2	1	1	1.03658	1.03658	2.07316	2.13114	0.0580
4	3	1	3.12029	1.03658	4.15687	4.26228	0.1054
6	3	3	3.12029	3.12029	6.24058	6.39342	0.1528
	5	1	5.22441	1.03658	6.26099		0.1324
8	5	3	5.22441	3.12029	8.34470	8.52456	0.1799
	7	1	7.34315	1.03658	8.37973		0.1448
10	5	5	5.22441	5.22441	10.4488	10.6557	0.2069
	7	3	7.34315	3.12029	10.4634		0.1923
	9	1	9.47048	1.03658	10.5071		0.1486
12	7	5	7.34135	5.22441	12.5677	12.7868	0.2193
	9	3	9.47048	3.12029	12.5908		0.1961
	11	1	11.6009	1.03658	12.6375		0.1494
14	7	7	7.34315	7.34315	14.6863	14.9180	0.2317
	9	5	9.47048	5.22441	14.6949		0.2231
	11	3	11.6009	3.12029	14.7212		0.1968
	13	1	13.7309	1.03658	14.7675		0.1505
16	9	7	9.47048	7.34315	16.8136	17.0491	0.2355
	11	5	11.6009	5.22441	16.8253		0.2238
	13	3	13.7309	3.12029	16.8512		0.1979
	15	1	15.8622	1.03658	16.8988		0.1503
18	9	9	9.47048	9.47048	18.9410	19.1803	0.2393
	11	7	11.6009	7.34315	18.9441		0.2362
	13	5	13.7309	5.22441	18.9553		0.2250
	15	3	15.8622	3.12029	18.9825		0.1978
	17	1	17.9946	1.03658	19.0312		0.1491
20	11	9	11.6009	9.47048	21.0714	21.3114	0.2400
	13	7	13.7309	7.34315	21.0741		0.2373
	15	5	15.8622	5.22441	21.0866		0.2248
	17	3	17.9946	3.12029	21.1149		0.1965
	19	1	20.1231	1.03658	21.1597		0.1517
22	11	11	11.6009	11.6009	23.3018	23.4425	0.2407
	13	9	13.7309	9.47048	23.2014		0.2411
	15	7	15.8622	7.34315	23.2054		0.2371
	17	5	17.9946	5.22441	23.2190		0.2235
	19	3	20.1231	3.12029	23.2434		0.1991
	21	1	22.2548	1.03658	23.2914		0.1511

TABLE I. Lengths of the diffractive orbits. The columns are: N = number of half-bounces in orbit; N_1 = number of half-bounces in first leg; N_2 = number of half-bounces of second leg; L_1 = length of first leg; L_2 = length of second leg; $L_{\text{tot}} = L_1 + L_2$; L_{hor} = length of horizontal orbit; $\Delta = L_{\text{hor}} - L_{\text{tot}}$. The configuration of the resonator for this data was $D = 1.0656R$, $\alpha = 115^\circ$. All numbers are given in terms of the radius of curvature of the reflector, which is taken to be unity.

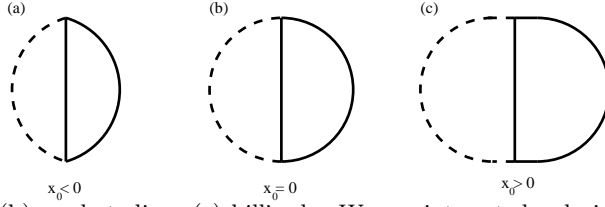


FIG. 23. The lemon (a), circle (b), and stadium (c) billiards. We are interested only in states of these billiards which are even about the x -axis, and odd about the y -axis.

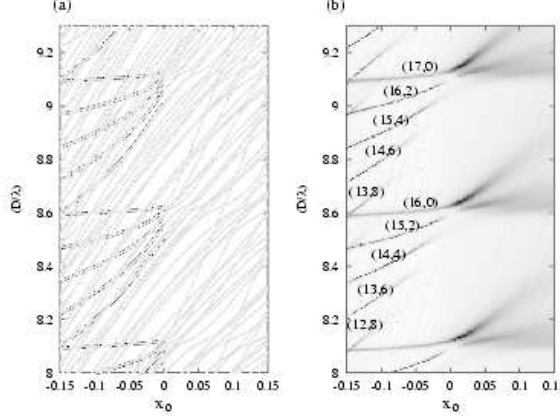


FIG. 24. On the left, the states of a closed billiard are shown, as the parameter x_0 is varied. For $x_0 < 0$, the billiard is a lemon billiard; for $x_0 = 0$, it is a circle; for $x_0 > 0$ it is a stadium. For $x_0 < 0$, we have darkened the lines corresponding to the allowed states of the corresponding open system (see Fig. 25 for the corresponding eigenfunctions). On the right, the experimental transmission spectra for the open system are shown for the same parameter range. Note the similarity of the figures in the range $x_0 < 0$, where the open system exhibits stable classical dynamics.

In the stable regime, imagine closing the QPC aperture and increasing the open angle of the arc-shaped reflector until it touches the straight wall. The resulting shape is one-half of a lemon billiard (see Fig. 23(a)). The shape of the lemon billiard is determined by the parameter $x_0 \equiv (D - R)/R < 0$, which is the x -value of the center of curvature of the arc on the right in units of the radius of curvature. The lemon billiard has been studied before [9,10]; for our purposes it is important that the classical dynamics in the lemon billiard is dominated by a large regular region.

As x_0 is increased to 0, the area enclosed by the arc becomes half of a perfect circle, and the closed system becomes completely integrable (see Fig. 23(b)). The eigenstates of a circular billiard are J -type Bessel functions.

Finally, as x_0 is made positive, the semicircular arc can be extended with horizontal straight segments to form half of a stadium billiard. The classical dynamics in the stadium billiard is completely chaotic. See Fig. 23(c).

The eigenstates of these three systems share certain properties with the scattering states of our open system. In these closed systems, there are no wall ends so we expect diffraction to play a smaller role in the energies and wavefunctions.

The similarity between these closed systems and our resonator is greatest in the stable regime. In this regime, the states of the resonator are essentially the same as the states of the lemon billiard that are even about the x -axis, and odd about the y -axis. (The straight wall in the resonator lies on the y -axis, thus enforcing a node there, while the symmetric position of the antenna means that it only excites states that are even about the x -axis.) As the reflector position is varied, we correspondingly change the parameter $x_0 < 0$ of the lemon billiard, and compare the states of each system. In the experiment, we see an avoided crossing at $x_0 = 0$. To investigate this, we can follow the states of the lemon/stadium billiard as the parameter x_0 is swept slowly through zero.

In Fig. 24(a) we plot the (even-about- x , odd-about- y) levels of the lemon/stadium billiard as a function of the parameter $x_0 = (D - R)/R$ and wavelength. On the right, the corresponding experimental transmission spectra for the open system are shown. Notice the exact matching of the transmission peaks with the lemon billiard states in the stable regime. This excellent agreement is an artifact of the fact that, while our resonator is a geometrically *open* system, it is classically *closed*, in the sense that almost all trajectories beginning at the QPC that hit the reflector are doomed to forever remain in the region between the wall and the reflector. We only begin to notice the “openness” of our resonator for the peaks corresponding to large numbers of angular nodes. As we shall see, such states have a large angular spread, and it grows with decreasing x_0 , so that eventually the caustics of the classical orbits supporting

these states approach the tip of the reflector. When this happens, the states broaden and disappear. For example, this is apparent for the peak with quantum numbers (13,8) at around $x_0 = -0.1$. The wavefunction corresponding to this peak has 13 radial nodes between the y -axis and the reflector, and 8 angular nodes. The states with fewer angular nodes do not have such a wide angular extent, and therefore they do not disappear from the spectra until the reflector is farther from the wall.

It is apparent that there are many states in the closed lemon billiard that do not appear at all in the analogous open system. All such states have considerable amplitude near the walls of the lemon billiard that are ‘missing’ from the open resonator—therefore in the open system the analogous states escape the resonator immediately. Thus they are absent in the experimental transmission spectra.

At $x_0 = 0$, there is an avoided crossing in both the open and closed systems. However, we see that the level repulsion is stronger in the open system. For example, observe the level repulsion of the states (17,0) and (16,2). The distance of closest approach of these two levels is four times greater in the open system than in the closed system. (For the open system, we judge the distance between the “levels” as the distance between the peak maxima.) Now, the major difference between the two systems as far as the eigenstates are concerned is the presence of diffractive orbits in the open case. Semiclassically speaking, there are diffractive paths that go from one state to the other and introduce a coupling that increases the level splitting. Therefore, we believe that the avoided crossing is in large part mediated by *diffraction* in the open system.

For $x_0 > 0$, the correspondence between the closed and open systems comes to a somewhat abrupt halt. This is apparent in Fig. 24. The reason is as follows. In the closed system, orbits with times up to about the Heisenberg time, $t_H \equiv 1/\Delta E$, affect the properties of the quantum states. In the open system, on the other hand, only a few orbits from a very specific part of phase space stay in the system for more than a few bounces. Therefore, we can expect states of the closed and open systems to correspond only if a significant subset of trajectories remains in the non-escaping region of phase space for roughly the Heisenberg time. Trajectories that leave that region of phase space explore parts of phase space where the systems differ and the correspondence breaks down. For the circle billiard at our experimental parameters, the particle makes approximately 7 horizontal bounces within the Heisenberg time of the quarter-stadium.

Using the 2D density of states, we can estimate the range of x_0 for which we may expect rough correspondence between the eigenstates of the closed system with the resonances of the open system in the unstable regime. There is another characteristic time, t_λ , which we will call the Lyapunov time, which is the characteristic time that it takes for a trajectory to “fall off” the horizontal periodic orbit. We expect correspondence when $t_H \lesssim t_\lambda$. The Lyapunov time is

$$t_\lambda = \frac{L}{k\lambda_{\text{Lyap}}}, \quad (15)$$

where L is the length of the periodic orbit, λ_{Lyap} is the Lyapunov exponent of the orbit, and k is the wavenumber (L/k is the period of the orbit). We will focus on the horizontal orbit for the case where the system is just barely unstable, so that $L \approx 2R$. The Lyapunov exponent for the horizontal orbit is given by the logarithm of the largest eigenvalue of the monodromy matrix, linearized about the horizontal orbit,

$$M = \begin{pmatrix} 1 + 2x_0 & 2x_0(1 + x_0) \\ 2 & 1 + 2x_0 \end{pmatrix} \quad (16)$$

[11]. The largest eigenvalue of this matrix is given by

$$\begin{aligned} m_+ &= 1 + 2x_0 + 2\sqrt{x_0(1 + x_0)} \\ &\approx 1 + 2\sqrt{x_0}, \end{aligned} \quad (17)$$

for small x_0 . Thus the Lyapunov exponent is

$$\begin{aligned} \lambda_{\text{Lyap}} &\approx \ln(1 + 2\sqrt{x_0}) \\ &\approx 2\sqrt{x_0}. \end{aligned}$$

Therefore, the Lyapunov time for the horizontal orbit is approximately

$$t_\lambda \approx \frac{R}{k\sqrt{x_0}}. \quad (18)$$

Eigenstates of the closed system				
(n, m)	$x_0 = -0.2$	$x_0 = 0.0$	$x_0 = 0.02$	$x_0 = 0.2$
(17,0)	71.3806	57.3275	56.8273	51.8407
(16,2)	70.2283	57.2577	56.4768	51.6105
(15,4)	69.0855	57.1173	56.2240	51.3391
(14,6)	67.9527	56.9052	56.1205	50.2602
(13,8)	66.8308	56.6196	55.8705	50.7444

TABLE II. Eigenvalues k for the states shown in Fig. 25. The quantum numbers in the first column are only good when x_0 is negative or a small positive number. In the stadium regime, the classical dynamics is chaotic and there are no longer any good quantum numbers; hence the quantum number assignment for $x_0 = 0.2$ is only an indication of its adiabatic ancestor for smaller values of x_0 . Note also that in the quantum numbering system, we do not count the angular node along the y -axis. This is to keep the analogy with the open system, where that node is trivial as it is forced by the position of the wall.

This must be compared with the Heisenberg time, which is $t_H = A/2\pi = R^2/8$ (the effective area of the billiard is $A = \pi R^2/4$ because of symmetry—we only take one quarter of the area of a full circle). We expect the correspondence between the open and closed systems to break down when these times are of the same order. That is, we look for the value of x_0 for which $t_H \approx t_\lambda$, which is

$$x_0 \approx \left(\frac{8}{kR} \right)^2. \quad (19)$$

Now, in our energy range $kR \approx 18\pi$. Thus we have for the value of x_0 at which correspondence ceases to hold,

$$x_0 \approx \left(\frac{8}{18\pi} \right)^2 \approx 0.02 \ll \frac{\lambda}{R}. \quad (20)$$

As indicated, this value of x_0 is much less than a wavelength, scaled to the radius of the billiard. This means that the states of the closed billiard already have mixed through a number of avoided crossings by the time the circle has been “stretched” by one wavelength. Indeed in Fig. 24 we see that the first avoided crossings are happening already near $x_0 = 0.02$, consistent with our rough estimate.

A sampling of states for the closed system of the lemon/stadium billiard is shown in Fig. 25. In this figure, the states corresponding to the series of quantum numbers (17,0) to (13,8) are shown, as the transition from a lemon to a stadium is made. The corresponding values of k for each state shown are given in Table II. The value of x_0 is given at the top of each column. We see that the angular extent of the lemon billiard states increases with the number of angular nodes, as mentioned previously. As x_0 approaches zero, the angular extent of each state is fully developed and covers the entire billiard, as is required by the rotational symmetry of the circle billiard states. The transition from the first to the second column is *adiabatic*, that is, from left to right we track the states with the same character.

In the third column, we have plotted the states after x_0 has been *adiabatically* increased to the small value $x_0 = 0.02$, such that they still bear some resemblance to the states of the circle. This parameter value was chosen to be just before the first avoided crossing in the closed system, in accordance with the discussion above. This effectively means that the periodic orbits are not too different from those of a circle billiard; i.e., the periodic orbits are only weakly unstable. This means that one may still draw analogies between the closed and open systems in this regime, although the character of a particular resonance in the open system may be shared by several states in the corresponding closed system. For example, note that the first two states in the third column have angular lobes which are qualitatively similar to the diffractive state shown in Fig. 6. On the other hand, the third and fourth states in that column have amplitude running from the center out along the x -axis, qualitatively similar to the Fabry-Perot type state in Fig. 6. There is even the appearance of a focus just to the right and left of the center of the billiard in these two states, analogous to the focus seen in the Fabry-Perot state for the open system.

In the last column, we plot the five wave functions after the parameter x_0 has been adiabatically increased to $x_0 = 0.2$, or 20% of the radius of curvature. Now we see that the states no longer have anything to do with the states of the open system, exactly for the reasons given above.

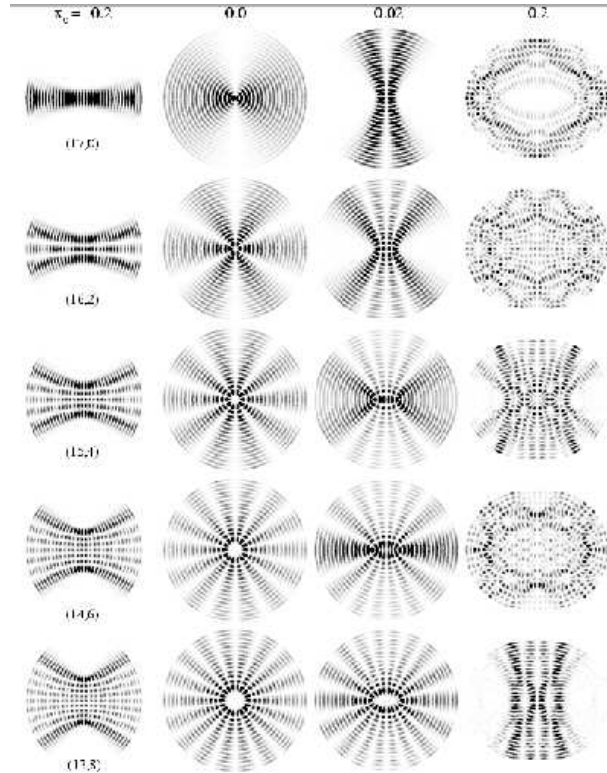


FIG. 25. Eigenfunctions of the lemon/stadium billiard. On the top line is shown the parameter x_0 , which describes how far the billiard is from a circle. On the left, we show some lemon billiard eigenfunctions, together with their quantum numbers. To the right, we show the eigenfunctions associated with each lemon state, as the parameter x_0 is varied adiabatically to $x_0 = 0, 0.02, 0.2$.

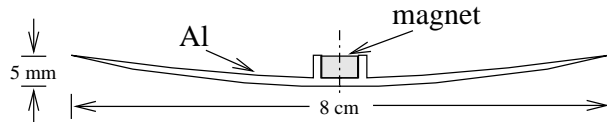


FIG. 26. A cross section down a diameter of the coarse probe used for measuring the microwave field. It has cylindrical symmetry about the center axis.

IX. IMAGING WAVEFUNCTIONS WITH A COARSE PROBE

We end this paper with an interesting discovery which was made in the course of carrying out the measurements described above: namely, the possibility of measuring an electronic wavefunction in a 2DEG. The viability of measuring pure state wavefunctions in the context of microwave billiard systems has been demonstrated by many authors [13–16]. However, the imaging of a wavefunction in a *real* quantum system has not yet been achieved.

We believe a technique similar to the method used here could be applied in clean mesoscopic systems to obtain images of two dimensional wavefunctions in a 2DEG. In such systems, the fermi wavelength λ of the electrons is on the order of 50 Å. In analogy to the steel ball used in the microwave experiments, an AFM tip held close to the surface of the heterostructure could serve as a perturbation to measure the frequency shifts. However, the perturbation due to a nearby AFM tip on the electron wavefunction is a smooth potential disturbance 50-100 Å in size, comparable to or greater than λ . One might expect that it would be difficult to measure the nodal lines of a wavefunction with such a coarse probe. To investigate this problem, we tried measuring a microwave mode with a coarse probe. Instead of the small steel ball, we used a probe 8 cm in size, corresponding to 1.5 wavelengths, for these measurements. The probe is shown in Fig. 26. It approximately a “chord” of a sphere. The probe could be moved around the upper surface of the top plate of the cavity by means of an external magnet, in a manner similar to that used for the steel ball perturbation. For a discussion of the form of the perturbation caused by this probe, see Appendix B.

The results of a wavefunction measurement of the peak $d1$ with the coarse probe are displayed in Fig. 27. Only half of the wavefunction was measured. For comparison, the same state as measured by the 4 mm ball is shown as well.

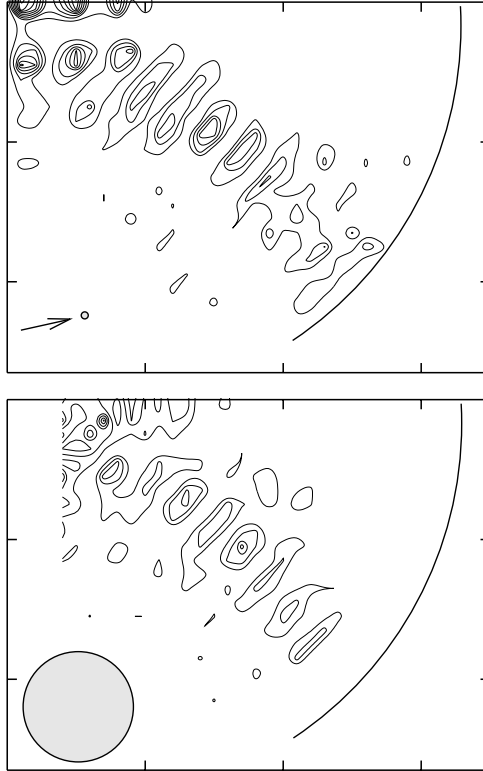


FIG. 27. A comparison between fine and coarse measurement probes. The sizes of the probes are indicated by circles in the lower left corner of each graph. In the upper plot, an arrow marks the probe. The tics on all axes are 10 cm apart.

Note that far from the QPC, the nodal lines in the two measurements match very well. For the coarse measurement, data near the wall and mirror were unavailable because of the large size of the probe. The level of detail obtained with the coarse probe is surprising, considering that it was over *three* half-wavelengths in diameter. This result suggests it might be possible to directly image an electron wavefunction in a 2DEG. A perturbative analysis of the effect of the coarse probe is presented in Appendix B.

X. CONCLUSION

In summary, we have demonstrated the existence of diffractive orbits in an open microwave billiard, which give rise to resonances and wavefunctions that would not be predicted by a simple semiclassical theory. Such orbits are of importance in open, unstable systems where the number of unstable classical periodic orbits is small. In such systems, diffraction can play a major role in determining the spectrum of the system. Furthermore, we have shown that it may be possible to measure the pure state wavefunction of an electron in a 2DEG, by using a coarse AFM tip as a probe.

This work was supported by NSF Grant CHE9610501. We are grateful to the Hewlett Packard Corporation for the loan of a network analyzer that was used in these experiments. We thank J. D. Edwards for the computer program that generated the exact quantum mechanical wavefunctions.

APPENDIX A: MASLOV INDICES

In the experiment, the antenna is placed very close to, but not exactly at, the wall. This means there are in fact *four* orbits associated with each single orbit in the billiard when the source is placed exactly at the wall. The four orbits associated with the shortest horizontal orbit are shown in Fig. 28. Each orbit in this family has a different total Maslov index and length, summarized in Table III. We can find the effect of grouping these four orbits into a single orbit by computing the following sum,

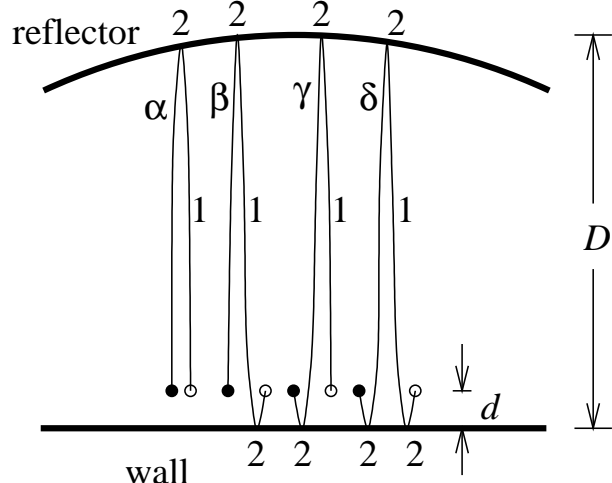


FIG. 28. Four orbits associated with the shortest horizontal orbit when the antenna is displaced from the wall. The trajectories start from the filled circles and end on the open circles. These circles are really the same point, namely the antenna position; they are displaced from each other in the figure so that the four distinct paths are visible. The Maslov indices acquired on each segment of each orbit are indicated. The antenna is a distance d away from the wall, and the horizontal distance from the wall to the reflector is D .

Family of horizontal orbits		
orbit	length	Maslov index
α	$2(D - d)$	3
β	$2D$	5
γ	$2D$	5
δ	$2(D + d)$	7

TABLE III. Lengths and Maslov indices for the orbits shown in Fig. 28.

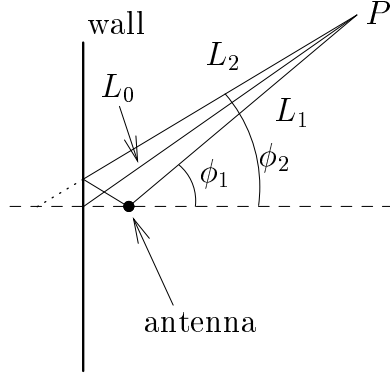


FIG. 29. Two trajectories arriving at the antenna from slightly different angles. The antenna is a distance d from the wall, as in the previous discussion.

$$Ae^{iS_{\text{eff}}-i\pi\mu_{\text{eff}}/2} = \sum_{n=\alpha,\beta,\gamma,\delta} e^{iS_n-i\pi\mu_n/2}, \quad (\text{A1})$$

where the sum is over the four orbits as $d \rightarrow 0$. The coefficient A will be found by doing the sum. We have

$$\begin{aligned} Ae^{iS_{\text{eff}}-i\pi\mu_{\text{eff}}/2} &= e^{2ik(D-d)-3\pi i/2} + 2e^{2ikD-5\pi i/2} \\ &\quad + e^{2ik(D+d)-7\pi i/2} \\ &= e^{2ikD-5\pi i/2} (2 - e^{2ikd} - e^{-2ikd}) \\ &= e^{2ikD-5\pi i/2} (2 - 2\cos(2kd)) \\ &\approx (2kd)^2 e^{2ikD-5\pi i/2}. \end{aligned} \quad (\text{A2})$$

Thus we have that $A = (2kd)^2$, $\mu_{\text{eff}} = 5$, and $S_{\text{eff}} = 2kD$, as expected.

A similar analysis on orbits coming to the antenna at an angle shows that the coupling to the antenna varies as $\cos\phi$, as stated in Eq. (9). Referring to Fig. 29, a source of rays begins at the point P , and two of the rays find their way to the antenna. The direct path has length L_1 and Maslov index $\mu_1 = 0$. The second path first bounces off the wall before arriving at the antenna, and has length L_2 and Maslov index $\mu_2 = 1$. We want to combine these two paths into a single trajectory, by doing a sum over the two trajectories as was done above, in order to find the effective action and Maslov index for the trajectory. We further define the length L_0 , which is the distance between P and the intersection of the wall with the axis of symmetry. The two lengths L_1 and L_2 are given by

$$\begin{aligned} L_{1,2} &= \sqrt{(L_0 \cos \phi \mp d)^2 + (L_0 \sin \phi)^2} \\ &\approx L_0 \mp d \cos \phi, \end{aligned} \quad (\text{A3})$$

where ϕ is the angle between the trajectory L and the x -axis, and $-$ and $+$ correspond to trajectories 1 and 2, respectively. The sum over orbits is then

$$\begin{aligned} e^{iS_{\text{eff}}-i\pi\mu_{\text{eff}}/2} &= e^{iS_1} + e^{iS_2-i\pi} \\ &= 2 \cos(kd \cos \phi - i\pi/2) e^{ikL_0-i\pi/2} \\ &\approx 2kd \cos \phi e^{ikL_0-i\pi/2}. \end{aligned} \quad (\text{A4})$$

As expected, the effective action for the two paths is just $S_{\text{eff}} = kL_0$, and the Maslov index is $\mu_{\text{eff}} = 1$. The factor $\cos\phi$ appearing above is exactly the angular dependent coupling coefficient appearing in Eq. (9). This is just the simple angular dependence of a p -wave point source.

APPENDIX B: EFFECT OF A COARSE PROBE

In this section we derive an effective potential describing the perturbation to a TEM microwave resonance due to a coarse probe. For simplicity we consider the case of a closed cavity. The electric field $\mathcal{E}(\mathbf{r}, t) = \text{Re} \mathbf{E}(\mathbf{r}) e^{-i\omega t}$ and magnetic field $\mathcal{B}(\mathbf{r}, t) = \text{Re} \mathbf{B}(\mathbf{r}) e^{-i\omega t}$ of such a state can be expressed in terms of the quantum analogue state, $\psi(x, y)$, as follows:

$$\mathbf{E}(x, y, z) = \frac{1}{h^{1/2}} \psi(x, y) \hat{\mathbf{z}} \quad (\text{B1})$$

$$\mathbf{B}(x, y, z) = \frac{1}{h^{1/2}} \frac{1}{ik} \left[\frac{\partial \psi}{\partial y} \hat{\mathbf{x}} - \frac{\partial \psi}{\partial x} \hat{\mathbf{y}} \right]. \quad (\text{B2})$$

The height of the cavity in the z -direction is denoted by h . (We use the normalization conventions $\int dx \int dy \psi^2 = \int d^3 \mathbf{r} |\mathbf{E}|^2 = \int d^3 \mathbf{r} |\mathbf{B}|^2 = 1$.)

The perturbation to the frequency of a microwave resonance by a conducting probe is [17]

$$\frac{\omega^2 - \omega_0^2}{\omega^2} = \int_{\Delta V} d^3 \mathbf{r} (|\mathbf{B}(\mathbf{r})|^2 - |\mathbf{E}(\mathbf{r})|^2) \quad (\text{B3})$$

$$= \frac{1}{h} \int dx \int dy \delta h \left[\frac{1}{k^2} (\nabla \psi)^2 - \psi^2 \right], \quad (\text{B4})$$

where ω_0 is the unperturbed frequency and $\delta h(x, y)$ is the thickness of the probe. The volume integral is over the volume excluded by the probe; the second line follows because the fields have no z -dependence. From the chain rule and the Helmholtz equation,

$$\begin{aligned} \delta h (\nabla \psi)^2 &= \nabla \cdot [\delta h \psi \nabla \psi - \frac{1}{2} \nabla (\delta h) \psi^2] \\ &\quad + k^2 \delta h \psi^2 + \frac{1}{2} \nabla^2 (\delta h) \psi^2. \end{aligned} \quad (\text{B5})$$

Substitute Eq. (B5) into Eq. (B4). Since δh is localized away from the lateral boundaries of the cavity, the surface terms of Eq. (B4) vanish and we are left with

$$\frac{\omega^2 - \omega_0^2}{\omega^2} = \frac{1}{k^2} \int dx \int dy \frac{1}{2} \frac{\nabla^2 (\delta h)}{h} \psi^2. \quad (\text{B6})$$

Therefore, to first order in perturbation theory, the coarse probe can be thought of as an effective perturbing potential of the form

$$V_{\text{eff}}(x, y) \propto \nabla^2 \frac{\delta h(x, y)}{h}. \quad (\text{B7})$$

Note that Eq. (B7) implies that the area integral of V_{eff} vanishes, which is a significant constraint on the type of potential that can be modeled by a conducting probe in a microwave cavity. In particular, the perturbation of a 2DEG by an AFM tip would not have this property.

In the case of our probe, $\delta h/h \approx f[1 - (\rho/\rho_0)^2]$ where ρ is the distance from the center of the probe, $\rho_0 = 40$ mm, and $f = 0.4$, so

$$V_{\text{eff}} \approx -\frac{4f}{\rho_0^2} + \frac{2f}{\rho_0} \delta(\rho - \rho_0); \quad (\text{B8})$$

in other words, the probe's effective potential is a flat well surrounded by a repulsive ring at the probe's circumference.

- [1] M. C. Gutzwiller, *Chaos in Classical and Quantum Mechanics* (Springer-Verlag, Berlin, 1990).
- [2] G. Vattay, A. Wirzba, and P. E. Rosenqvist, Phys. Rev. Lett. **73**, 2304 (1994).
- [3] N. Pavloff and C. Schmit, Phys. Rev. Lett. **75**, 61 (1995).

- [4] M. Sieber, N. Pavloff, and C. Schmit, Phys. Rev. E **55**, 2279 (1997).
- [5] N. Whelan, Phys. Rev. E **51**, 3778 (1995).
- [6] J. B. Keller, J. Opt. Soc. Am. **52**, 116 (1962).
- [7] J. S. Hersch, M. R. Haggerty, and E. J. Heller, Phys. Rev. Lett. **83**, 5342 (1999).
- [8] J. S. Hersch, Ph.D. thesis, Harvard University, 1999. Available at <http://monsoon.harvard.edu>.
- [9] J. A. Katine *et al.*, Phys. Rev. Lett. **79**, 4806 (1997).
- [10] E. J. Heller and S. Tomsovic, Physics Today **46**, 38 (1993).
- [11] J. D. Edwards, Ph.D. thesis, Harvard University, 1998. Available at <http://monsoon.harvard.edu>.
- [12] R. M. Westervelt, private communication.
- [13] S. Gokirmak, D. H. Wu, J. S. A. Bridgewater, and S. M. Anlage, Rev. Sci. Inst. **69**, 3410 (1998).
- [14] S. Sridhar, D. Hogenboom, and B. A. Willemsen, J. Stat. Phys. **68**, 239 (1992).
- [15] J. Stein and H. J. Stöckmann, Phys. Rev. Lett. **68**, 2867 (1992).
- [16] H. J. Stöckmann and J. Stein, Phys. Rev. Lett **64**, 2215 (1990).
- [17] L. C. Maier and J. C. Slater, J. App. Phys. **23**, 68 (1954).
- [18] G. L. James, *Geometrical theory of diffraction for electromagnetic waves* (Peregrinus, Stevenage, England, 1976), p. 115.
- [19] Note that the expression given in Ref. [18] is the complex conjugate of the expression above, because the convention for the time dependence of the fields taken in Ref. [18] is $e^{i\omega t}$, whereas we take the opposite convention, $e^{-i\omega t}$.
- [20] R. G. Kouyoumjian and P. H. Pathak, Proc. IEEE **62**, 1448 (1974).
- [21] The reason for the difference in the argument of the Fresnel integral is that in the half-line case the incident wave was plane ($l_1 \rightarrow \infty$), whereas in the present case the incident wave is a cylindrical wave emanating from the QPC.
- [22] S. Chan and E. J. Heller, Phys. Rev. Lett. **78**, 2570 (1997).
- [23] M. F. Crommie, C. P. Lutz, D. M. Eigler, and E. J. Heller, Physica D **83**, 98 (1995).
- [24] Strictly speaking, there *is* diffraction in the lemon and stadium billiards, although it is of a different nature than in the corresponding open system. In the lemon billiard, it occurs at the point where the two arcs meet, and there is a discontinuity of slope. In the stadium, it occurs at the point where the arcs meet the straight wall sections, and there is a discontinuity of curvature. Since the discontinuities are of higher order, diffraction is weaker than in the open system.